World Scientific
www.worldscientific.com

FINITE-ELEMENT MODELING OF A BEVEL-TIPPED NEEDLE INTERACTING WITH GEL

WISSAM ASSAAD, ALEX JAHYA, PEDRO MOREIRA
and SARTHAK MISRA*

Department of Biomechanical Engineering
MIRA-Institute for Biomedical Technology and Technical Medicine
University of Twente, Enschede, P.O. Box 217, 7500AE, The Netherlands
*s.misra@utwente.nl

Deviation of a needle from its intended path can be minimized by using a robotic device to steer the needle towards its target. Such a device requires information about the interactions between the needle and soft tissue, and this information can be obtained using finite element (FE) analysis. In this study, we present an FE analysis that integrates the Johnson–Cook damage model for a linear elastic material with an element deletion-based method. The FE analysis is used to model a bevel-tipped needle interacting with gel. The constants for the damage model are obtained using a compression test. We compare simulation results with experimental data that include tip–gel interaction forces and torques, and three-dimensional (3D) *in situ* images of the gel rupture obtained using a laser scanning confocal microscope. We quantitatively show that the percentage errors between simulation and experimental results for force along the insertion axis and torque about the bevel edge are 3% and 5%, respectively. Furthermore, it is also shown qualitatively that tip compression is observed at the same locations in both experimental and simulation results. This study demonstrates the potential of using an FE analysis with a damage model and an element deletion-based method to accurately simulate 3D gel rupture, and tip–gel interaction forces and torques.

Keywords: Finite element; damage model; element deletion; three-dimensional; microscopic; bevel-tipped needle; gel.

1. Introduction

One of the most common minimally invasive procedures performed is percutaneous needle insertion. It is routinely used for diagnosis (e.g., biopsy) and drug delivery (e.g., brachytheraphy). The benefit of minimally invasive procedures over open surgery is the reduced tissue trauma and patient recovery time.[1] During the percutaneous insertion procedure, accurate needle placement is of utmost importance

*Corresponding author.

since tip misplacement reduces conclusiveness and effectiveness of the diagnosis and treatment, respectively.[2] A needle might deviate from its intended path due to several reasons such as tissue deformation or physiological processes.[3] This deviation can be reduced by using a robotic system that is capable of predicting needle deflection, and also steering the needle towards the target.[4,5] Such a device requires knowledge of needle-tissue interactions which can be obtained through experiments or simulation-based methods such as finite element analysis.[6]

Previous work has investigated needle-tissue interactions through experiments.[2,7–10] Their results showed that several parameters such as needle insertion speed, bevel angle and diameter, and gel elasticity influence the interactions between needle and soft tissue. Microscopic observations done by Misra *et al.* also showed that needle insertion induces tip compression and gel rupture.[11] During needle insertion, variations in the parameters (i.e., insertion speed, bevel angle, etc.) result in changes in the coupling between tip compression and gel rupture.[12] Subsequently, these changes affect the tip–tissue interaction forces and needle deflection.

An finite element (FE) analysis can also be used to investigate needle–tissue interactions.[13] Such an analysis needs to take into account several factors i.e., material characterization, material rupture, geometry non-linearity (large deformation), and non-linear boundary conditions (contact). An FE simulation with cohesive zone algorithm can be used to simulate tip rupture.[3,14] Nevertheless, a cohesive zone model requires that the needle path is known prior to insertion. If the needle path is unknown, cohesive elements can also be distributed over a region where the needle is expected to deflect. However, the drawback of this method is the significant increase in the number of degrees-of-freedom and subsequently, the computational cost.[14] Another method proposed by Kong *et al.* is to use an FE model with an element deletion-based method.[15] The results of their study showed that the FE model can be used to simulate needle-tissue interaction forces. In their simulations, a micro-needle was inserted into a 2D multilayer skin model, while in our work we apply the element deletion technique to the 3D case.

In this study, we use an FE analysis to simulate 3D gel rupture, and tip–gel interaction forces and torques. In the analysis, a Johnson–Cook damage model and an element deletion-based method are used. Further, compression test of the gel is used to obtain material mechanical parameters (Young's modulus and yield stress) and constants of the damage model. In general, gel exhibits non-linear elastic behavior. However, for the purposes of planning minimally invasive surgical procedures, our previous work has shown that the deformation response of non-linear elastic material is predominantly dependent on accurate modeling of boundary conditions, rather than the material properties.[16–19] Additionally, compression tests are performed and they show that the gel has a linear elastic behavior. Thus, in this study, a linear elastic FE model is used in the simulations. Furthermore, simulation results are compared with experimental data that include forces and torques exerted on the needle tip and 3D images of the gel rupture obtained using a Zeiss Laser Scanning Confocal Microscope (LSCM) 510 (Zeiss, Oberkochen, Germany). To the

best of the authors knowledge, this work is the first investigation of an FE analysis (with an element deletion-based method) for modeling 3D needle insertion into gel, and it is also the first comparison of simulation results with experimental data that include 3D *in situ* images of gel rupture. This study is an important step towards an accurate FE analysis for pre- and intra-operative needle insertion planning.

This paper is outlined as follows: Section. 2 describes both materials and methods used in the experiments in order to obtain parameters of the FE simulations. These parameters are coefficient-of-friction between needle and gel, elasticity, yield stress and plastic strain. Subsequently, Sec. 3 presents the qualitative and quantitative comparisons between simulation results and experimental data. Finally, Sec. 4 concludes with discussion and future work.

2. Experiments

First, Sec. 2.1 presents the experimental setup used for microscopic observations of tip-gel interactions. Second, Sec. 2.2 explains the compression test performed on gel samples. The analysis is utilized to obtain parameters of the gel used in the FE simulations. The technique used to obtain coefficient-of-friction between needle and gel is also described in this section. Last, Sec. 2.3 briefly explains how the FE analysis is used to simulate 3D gel rupture and tip–gel interaction forces.

2.1. *Materials and methods*

For this study, we use 2% agarose gel in the experiments. This gel is commonly used as an alternative to biological tissue in the drug delivery tests, and also as biomaterials.[21,22] Further, the 2% agarose results in a gel with elasticity commonly observed in fascia and ligaments.[23] The gel is prepared by mixing 1.0 g of agarose powder (Eurogentec S.A., Seraing, Belgium) in 50 mL of 1× tris-borate-ethylene-diaminetetraacetic acid (EDTA) buffer. Subsequently, the solution is heated to 100°C until the agarose powder is completely dissolved. Further, 100 μL fluorescein isothiocyanate (FITC) is added to increase the contrast in the microscopic observations between needle and gel during the experiments. Finally, the solution is poured into moulds and left to solidify at 5°C for 24 h.[24] Two types of gel-sample shapes are used: A cube and a cylinder. The dimensions of the cubic and the cylindrical gel samples are 12 mm (length × width × height), and 14 mm × 13 mm (diameter × length), respectively. The cylindrical gel sample is used in the compression tests (Sec. 2.2), while the cubic gel sample is utilized in microscopic observations.

The experimental setup for microscopic observations consists of a needle insertion device, a phantom support, and a Zeiss 510 LSCM (Fig. 1). A solid 45° bevel-tipped steel needle of 1 mm diameter and length of 20 mm (item #5, Fig. 1) is used during the experiments. The Young's modulus of the needle is 200 GPa. This needle is mounted on a six-axis Nano17 force/torque sensor (ATI Industrial Automation, Apex, USA) (item #6, Fig. 1). The force and torque resolution of the sensor are
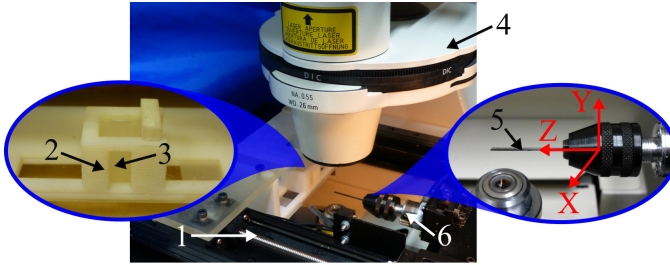
Fig. 1.   Experimental setup for microscopic observations. 1: Needle insertion device, 2: phantom support, 3: gel sample, 4: laser scanning confocal microscope, 5: needle and 6: Nano17 force/torque sensor. The needle is of 1 mm diameter and 45° bevel angle. Axis convention is also shown in the figure.

3.1 mN and 15.6 mN-mm, respectively. During the experiments, the gel sample is secured by a phantom support (item #2, Fig. 1), ensuring that the sample does not move during needle insertion. Thus, the Nano17 sensor only measures forces and torques between the needle and gel sample. The force and torque at the needle base are sampled at 2000 Hz using National Instrument's LabView™ data acquisition software (National Instruments Corporation, Austin, USA).

Furthermore, experimental procedures are as follows: Initially, the needle is inserted by 1 mm in order to ensure that its tip is embedded in the gel sample. The needle is pre-inserted into the gel sample to allow the visualization of the region of interest by the LSCM microscope. Subsequently, the needle is inserted by 0.5 mm and during this insertion, tip-gel interaction forces and torques are recorded. Since the focus of this study is to model the tip rupture process, and due to space and imaging constraints of the LSCM, 0.5 mm needle insertions are performed. For all experiments, needle insertion speed is 1.0 mm/s. During insertion, tip rupture is observed using a LSCM microscope, and 3D tip rupture images are obtained with an image resolution of 512 pixels × 512 pixels. The LSCM generates the 3D image by stacking a series of 2D images separated by 10 μm.[20] Further, needle-gel interactions are visualized with differential interference contrast (DIC), epifluorescence using the 488 nm line of the argon laser and a 10× objective lens. Compression test on gel samples is also performed to acquire parameters of the gel used in the FE analysis.

2.2. *Gel parameters acquisition*

2.2.1. *Compression test*

Parameters such as gel elasticity, yield stress and plastic strain are used in the FE analysis to simulate gel rupture during needle insertion. These parameters are obtained using compression test on cylindrical gel samples (Fig. 2). During the experiments, the cylindrical gel sample is carefully positioned between the loading plates of a rheometer (Anton Paar, Gentbrugge, Belgium) (item #2, Fig. 2). The boundary condition between the plates of rheometer and the gel sample are considered as surface-to-surface frictionless contact due to oil applied on the outer
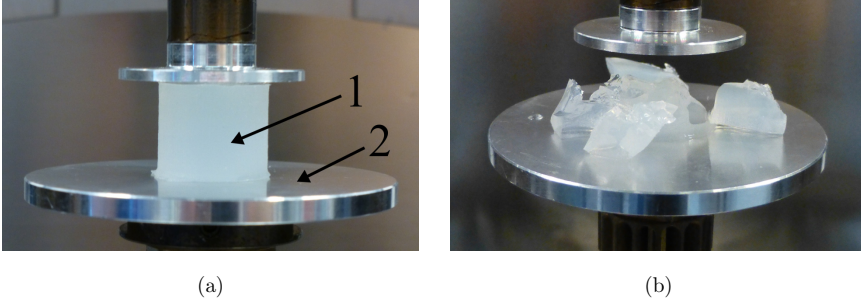
(a)   (b)

Fig. 2.   (a) Compression test of the cylindrical gel sample. 1: Cylindrical gel sample and 2: loading plates. (b) A completely damaged gel sample.

surfaces of the sample. Therefore, damage in the gel sample is due to a pure compressive exerted load. The tests are repeated five times, and mean values are reported. The gel sample is compressed at a speed of 0.1 mm/s with a strain rate of $\sim 0.008\,\mathrm{s}^{-1}$, while the rheometer measures the resulting force and displacement. For our gel samples, a compression test is preferable using the commercially-available rhoemeter.[25,26] Subsequently, this information is used to calculate true stress (σ) and true strain (ε) of the gel which are given by[27]:

$$\varepsilon = \ln\left(\frac{l}{l_0}\right) \quad \text{and} \tag{1}$$

$$\sigma = \frac{F \cdot l}{A_0 \cdot l_0}, \quad \text{where } A_0 \cdot l_0 = A \cdot l. \tag{2}$$

In Eq. (2), A_0 and A are the original and compressed cross-sectional area of the gel sample, respectively, while l_0 and l are the original and compressed length of the gel sample, respectively. Figure 3 provides a representative experimental result and the
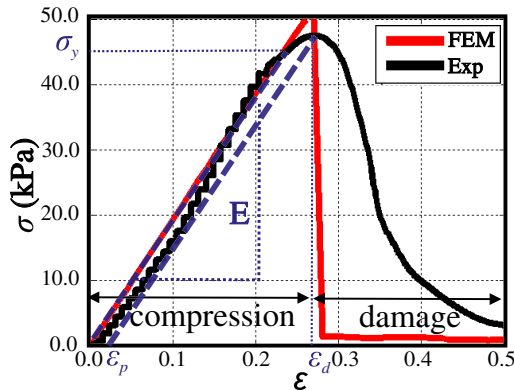

Fig. 3.   (Color online) Experimental result (black line) and finite element modeling (FEM) (red line) of true stress (σ) versus true strain (ε) for the cylindrical gel sample undergoing a compression test. E, σ_y, ε_p, and ε_d are gel elasticity, yield stress, plastic strain and damage strain of the gel sample, respectively.

Table 1. Parameters used in the finite element analysis. E, σ_y and ε_p are the gel Young's modulus, yield stress and plastic strain, respectively. The yield stress σ_y and plastic strain ε_p are obtained from the results of the compression test (Fig. 3).

Parameters	E (MPa)	σ_y (kPa)	ε_p
Values	0.27	49	0.004

FE simulation result of true stress versus true strain of the gel. The FE simulation is performed using the parameters presented in Table 1.

In general, soft tissues exhibit hyper-viscoelastic behavior.[28] However, based on the true stress and true strain data (Fig. 3), we assume that the gel sample is linearly elastic. The values of σ and ε are calculated from the results of the compression test. We observe that true stress is approximately linearly proportional to true strain prior to gel damage (compression region). It is also noted that gel compression after damage strain (ε_d) results in the sample being completely damaged (Fig. 2(b)). The derived parameters of the sample (i.e., gel elasticity (E), yield stress (σ_y), and plastic strain (ε_p)) are used in the FE analysis (Table 1).

2.2.2. *Coefficient-of-friction test*

The coefficient-of-friction parameter is obtained from experiments (Fig. 4) using the needle insertion device. Furthermore, forces at the needle base are recorded during the experiments using the Nano17 sensor.

In the experiments, the needle is initially inserted into the cubic gel sample at insertion speed of 1 mm/s. When the needle tip has completely passed through the gel sample, the insertion is stopped, the sensor is initialized to zero after the gel
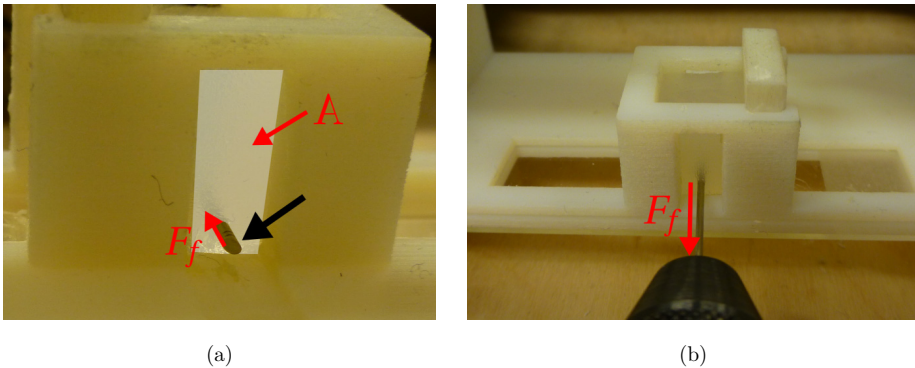

(a)　　　　　　　　　　　　　　　(b)

Fig. 4. Experiments to obtain coefficient-of-friction between the needle and gel. Forces are not acquired during this initial insertion. In (a), black arrow shows the needle tip and surface A indicates the gel surface punctured by the tip. (b) The needle is retracted and forces are recorded. In both figures, F_f represents the friction force along the needle shaft.

sample is allowed to relax. Forces are not acquired during this initial insertion. Subsequently, the needle is retracted at the same insertion speed, and the forces at the needle base are acquired. Coefficient-of-friction between needle and gel (μ) is calculated based on the experimental data collected when the needle is retracted, and by:

$$\mu = \frac{F_z}{F_x \cdot \cos(\theta) + F_y \cdot \sin(\theta)} \quad \text{and} \quad \theta = \tan^{-1}\left(\frac{F_y}{F_x}\right), \tag{3}$$

where F_x, F_y and F_z are the components of the resultant force along x-, y- and z-direction, respectively (Figs. 1 and 5). These forces are measured by the force sensor in the Cartesian coordinate system. The needle is cylindrical in shape. The friction force at the interface between the needle and gel sample is tangent to the needle outer surface and along the insertion direction. The normal force is perpendicular to the needle outer surface and pointing outward. The calculation of μ requires the friction and normal forces. The normal force is calculated by transforming the measured forces into a cylindrical coordinate system (*radial, azimuth, insertion*), where θ is the angle in the *azimuth* direction. Since the needle is not rotated, the force in the *azimuth* direction is equal to zero. The normal force is equal to the force along the *radial* direction. Further, the friction force is along the *insertion* direction. By transforming the forces in the cylindrical coordinate system to the Cartesian coordinate system, we obtain Eq. (3).

In the experiment (Fig. 5), during initial insertion, forces are not recorded. Subsequently, in phase I, the needle is retracted and forces are acquired. At longer
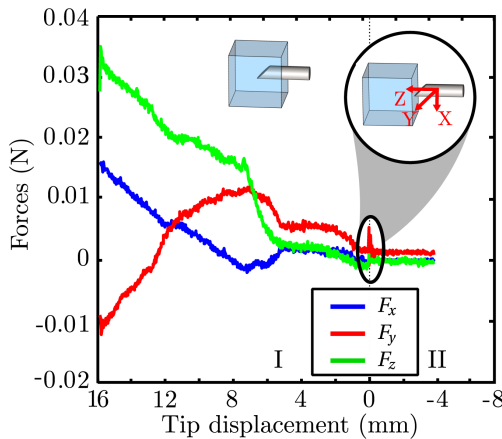

Fig. 5. Forces at the needle base (F_x, F_y and F_z) versus tip displacement. F_x, F_y and F_z are the components of the resultant force, measured by the force sensor, along x-, y- and z-direction, respectively (Fig. 1). Initially, the needle is inserted until its tip has completely passed through the gel sample. In phase I, the needle is retracted and forces are acquired. Bending forces (F_x and F_y) are dominant for longer (16–4 mm) insertion distances, while friction forces primarily acts along the needle shaft for insertion distance less than 4 mm. Phase II shows the region where the needle tip has been completely retracted out of the gel sample.

insertion distances (between 16 and 4 mm), the needle experiences larger bending forces (F_x and F_y). The recorded forces are assumed to be only due to friction forces along the needle shaft between 4 and 0 mm insertion distance. Phase II shows the region where the needle tip is out of the gel sample. Tip displacement is 0.0 mm when the tip just touches the gel sample. Coefficient-of-friction (μ) between the needle and gel is calculated based on the experimental data collected during phase I and at tip displacement of 4 mm. In this study, the calculated μ is 0.68 (Eq. (3)).

2.3. *Finite element analysis*

2.3.1. *Material damage model*

For the FE analysis, Abaqus/Explicit (Dassault Systémes Simulia Corporation, Providence, RI, USA) is used to simulate 3D gel rupture and tip–gel interaction forces. The gel rupture is simulated using an element-deletion based method. We use a meshing algorithm (as implemented in Abaqus/Explicit) in the FE analysis. Since the region of interest in this study is around the needle tip, the phantom model is partitioned such that the region where the needle penetrates the phantom has a radius equal to that of the needle. Partitioning the model reduces the total number of degrees-of-freedom, and subsequently the computational time. The needle and the gel sample are discretized with 8-node brick elements. As an input to the simulation, we specify the maximum global element size to be 0.5 mm. We get smaller elements in the cylindrical partition due to the non-flat/curved surfaces. In our model, the smallest element size is 0.05 mm. Furthermore, geometric non-linearity and a damage model are also taken into account in the FE analysis. The damage model is used to simulate gel damage initiation and evolution due to needle insertion.

In this study, we assume that the gel behaves as linear elastic material prior to gel rupture (before $\sigma_{\text{yield}} = 49\,\text{KPa}$) and has a Poisson's ratio of 0.495. This assumption is based on the results of the compression test of the cylindrical gel samples which show that true stress is approximately linearly proportional to true strain prior to gel damage (compression, Fig. 3). A Johnson–Cook damage model is utilized since it requires only a limited number of constants. These constants can be obtained from the results of the compression test of the gel. The damage model for gel fracture strain (ε^f) is defined by[29]:

$$\varepsilon^f = [D_1 + D_2 \mathrm{e}^{-D_3 \sigma^*}][1 + D_4 \ln \dot{\varepsilon}^*][1 + D_5 T^*], \tag{4}$$

where σ^* is pressure-stress ratio, $\dot{\varepsilon}^*$ is the dimensionless plastic strain rate for $\dot{\varepsilon}_0 = 1.0\,\text{s}^{-1}$, and T^* is the homologous temperature of the gel. Moreover, σ^* is given by

$$\sigma^* = \frac{\sigma_m}{\bar{\sigma}}, \tag{5}$$

while $\dot{\varepsilon}^*$ is defined as

$$\dot{\varepsilon}^* = \frac{\dot{\varepsilon}}{\dot{\varepsilon}_0}, \tag{6}$$

and T^* is calculated by

$$T^* = \frac{T}{T_m}. \tag{7}$$

where σ_m is the hydrostatic pressure applied to the gel and $\bar{\sigma}$ is the Von Mises stress. In Eqs. (6) and (7), $\dot{\varepsilon}$ is the strain rate, and T and T_m are the gel temperature at the start of compression test and the melting point temperature of the gel, respectively.

Modeling material failure requires damage initiation model and damage evolution. Johnson–Cook model (Eq. (4)) and energy-based damage evolution are used as damage initiation and damage evolution models, respectively.[30,31] The fracture energy is used as input in the damage evolution model, and it is assumed to be similar to that of gelatin, i.e., $8\,\mathrm{J/m^2}$.[27] The metric (D) is defined as the ratio of the equivalent plastic strain increment at each integration cycle to the gel fracture strain. When D reaches the critical value of 1, then an element is deleted and energy equivalent to the fracture energy is released.

In the FE analysis, only constant D_1 is used and the remaining constants (D_2, D_3, D_4 and D_5) are neglected. During compression test of the gel sample, it is noted that gel compression after ε_d results in the gel sample being completely damaged (Fig. 3). Hence, in our study, the effects of both σ^* and $\dot{\varepsilon}^*$ can be neglected (i.e., $D_2 = D_3 = D_4 = 0$). Furthermore, given that compression test of the gel sample is done at room temperature, the gel can also assumed to be isothermal (i.e., $D_5 = 0$). The constant D_1 is obtained from the results of compression test and its value is equivalent to $\varepsilon_{\mathrm{plastic}}$. In summary, D_1 is 0.041 while D_2, D_3, D_4, and D_5 are zero.

2.3.2. *Boundary conditions*

In the FE simulations, the needle is constrained in both x- and y-direction (Fig. 6), and displaced along the z-direction at insertion speed of $1\,\mathrm{mm/s}$. Moreover, the bottom gel surface ($P1$, Fig. 6) is fixed in all directions. Gel surfaces ($P3$ and $P4$) are constrained in x-direction, while $P2$ and $P5$ are fixed in z-direction. These constraints are applied according to boundary conditions of the gel during experiments (Fig. 1). Furthermore, the contact between the needle and gel is modeled with coefficient-of-friction of 0.68 (Eq. (3)). In the FE analysis, the needle is initially inserted at insertion depth of $1\,\mathrm{mm}$. Subsequently, the needle is inserted by $0.5\,\mathrm{mm}$, and during this insertion, tip–gel interaction forces are recorded. Simulation results are then compared with experimental data.
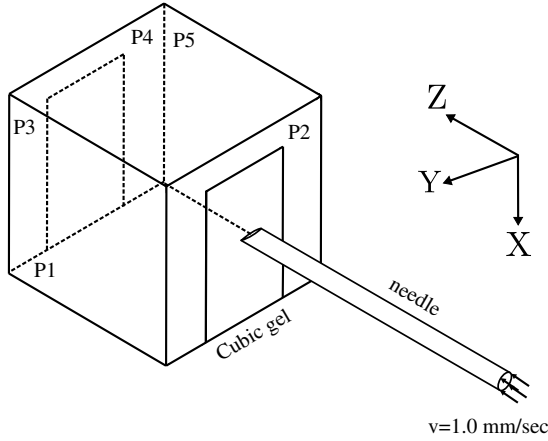
Fig. 6. A sketch of a needle inserted into a cubic gel sample. P1, P2, P3, P4 and P5 represent gel surfaces where fixed constraints are applied (Sec. 2.3.2). In the simulations, the needle is inserted at a speed (v) of 1 mm/s.

3. Results

The results of the FE analysis are compared with force/torque data and 3D images of gel rupture obtained using an LSCM. Force/torque data are recorded during needle insertion into the gel sample (up to insertion depth of 0.5 mm), while the images are taken when the insertion stops.

The experiment is repeated thrice. For each case, forces along x-, y- and z-direction, and torques about x-, y- and z-direction are plotted in Fig. 7. The RMS of
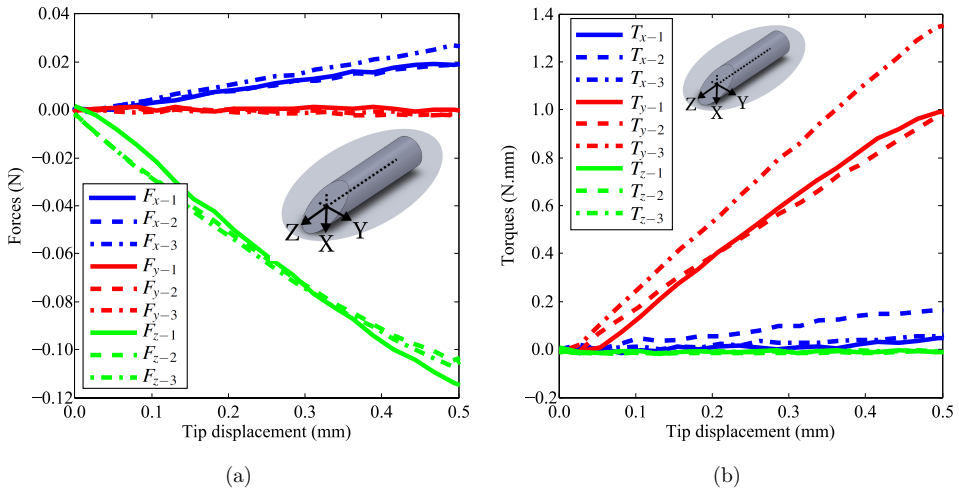

Fig. 7. Forces and torques for needle insertion depth of 0.5 mm. The plots show results of three experiments. F_{x-i}, F_{y-i} and F_{z-i} are the forces along x-, y- and z-direction, respectively. Moreover, T_{x-i}, T_{y-i} and T_{z-i} are the torques about x-, y- and z-direction, and i is the experiment number.
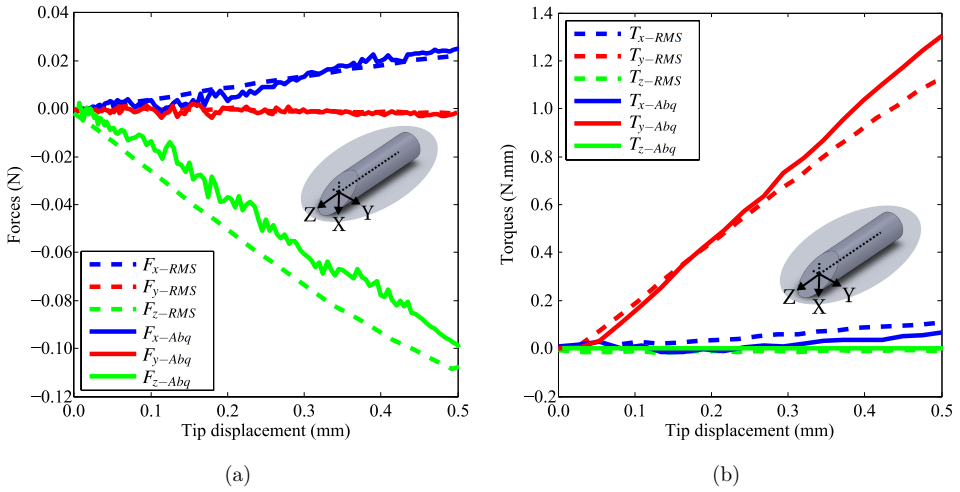
(a) (b)

Fig. 8.   Root mean square (RMS) of measured forces and torques for three experiments, and calculated forces and torques by FE analysis for needle insertion depth of 0.5 mm. $F_{x\text{-RMS}}$, $F_{y\text{-}RMS}$, $F_{z\text{-RMS}}$, $T_{x\text{-RMS}}$, $T_{y\text{-RMS}}$ and $T_{z\text{-RMS}}$ are RMS values of forces of three experiments along x-, y- and z-direction, and the RMS values of torques about x, y and z-direction, respectively. $F_{x\text{-Abq}}$, $F_{y\text{-Abq}}$, $F_{z\text{-Abq}}$, $T_{x\text{-Abq}}$, $T_{y\text{-Abq}}$ and $T_{z\text{-Abq}}$ are forces calculated by FE analysis along x-, y- and z-direction and torques calculated by FE analysis about x, y and z-direction, respectively. The errors at the end of the insertion between the RMS results and the FE analysis are 3.11×10^{-3} N, 2.07×10^{-6} N and 1.03×10^{-2} N for the forces in x-, y- and z-direction, and 5.07×10^{-2} N-mm, 1.92×10^{-1} N-mm and 6.92×10^{-3} N-mm for the torques about x-, y- and z-direction, respectively.

measured forces and torques of the three experiments and the FE analysis are plotted in Fig. 8. Experimental data are obtained using Nano17 force/torque sensor that is located at the needle base. Figure 9 presents the results of the FE analysis and one representative experimental result (Experiment #3). The maximum error of F_x, F_y and F_z are 9.0×10^{-3} N, 4.9×10^{-3} N, 0.02 N, respectively. Moreover, the maximum error of T_x, T_y and T_z are 0.05 N-mm, 0.20 N-mm, and 0.00 N-mm, respectively. In Experiment #3, the percentage errors between the FE simulations and the experimental data at the end of the insertion for force along the insertion direction (z-direction) and torque about the bevel edge (y-direction) are 3% and 5%, respectively.

Qualitatively, 3D images of gel rupture from the results of FE simulations are compared with the images obtained during experiments. Microscopic observation is done at a plane parallel to the bottom surface ($P1$, Fig. 6) and at the location where the tip image is sharp. Subsequently, this location from $P1$ is noted and used to correlate 3D images obtained from the results of FE simulations. These images are provided in Fig. 10. It is shown that an FE model with an element deletion method can be used to simulate gel rupture due to needle insertion. Arrows in Fig. 10 shows the locations where tip compression occurs. The simulation incorporates non-linear boundary conditions. In the results of FE analysis, tip compression is defined as the area where large displacements are noted (i.e., red region, Fig. 10(b)).
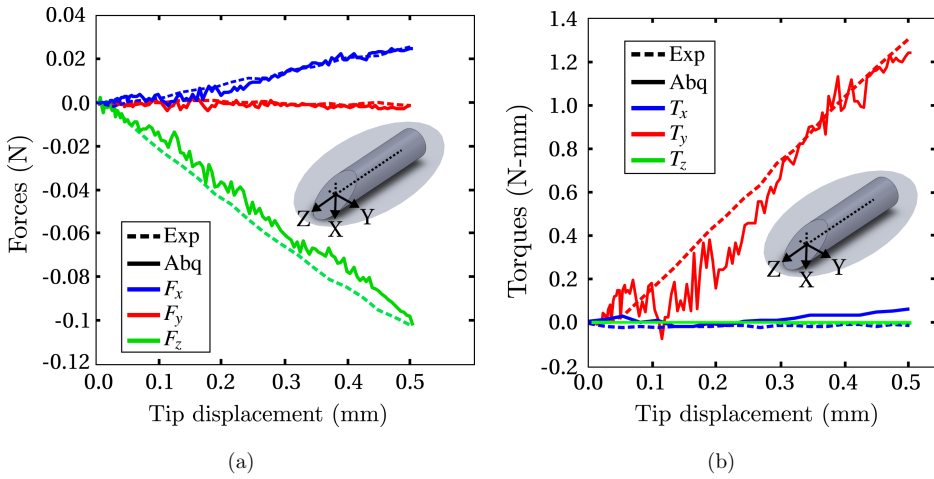
(a)   (b)

Fig. 9. Comparison between one representative experimental result and simulation results. F_x, F_y, F_z are the forces along x-, y- and z-direction, respectively, while T_x, T_y and T_z are the torques about x-, y- and z-direction, respectively. Exp is the experimental result and Abq is the simulation result. The maximum error between simulation and experimental results of F_x, F_y, F_z, T_x, T_y and T_z are 9.0×10^{-3} N, 4.9×10^{-3} N, 0.02 N, 0.05 N-mm, 0.20 N-mm, and 0.00 N-mm, respectively.

A sensitivity study is also performed to investigate the effect of reducing global mesh size on the results of FE simulations. It is noted that further reduction of mesh size did not improve the results of FE simulations. However, a finer mesh does significantly increase the computational time.
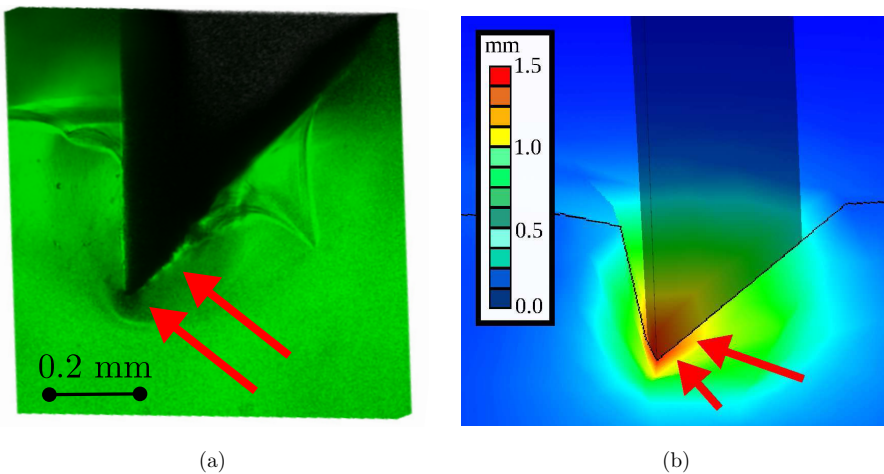

(a)   (b)

Fig. 10. (a) (Color online) Three-dimensional *in situ* image of gel rupture acquired using a laser scanning confocal microscope. (b) Contour plot of nodal displacements obtained from FE simulation results. Red arrows show the locations where tip compression is observed.

4. Conclusion

In this study, we compare experiment and FE simulation for investigating needle–tissue interaction. For simulating needle insertion into gel, we use an FE analysis with a Johnson–Cook damage model for a linear elastic material and an element-deletion method. Furthermore, compression test of the gel is used to obtain constants of the damage model. We compare simulation results with experimental data that include both force and torque data, and 3D images of gel rupture. These 3D *in situ* images are obtained during needle insertion into cubic gel samples and using a LSCM.

The results of our study show that the FE model can be used to accurately simulate 3D gel rupture, and tip–gel interaction forces and torques. Quantitatively, the percentage errors between FE simulations and experimental results for force along the insertion axis and torque about the bevel edge are 3% and 5%, respectively. Qualitatively, tip compression is noted at the same locations in both FE simulation and experimental results.

4.1. *Future work*

For future work, we plan to extend the results of this study to include needle deflection with longer insertion distances.[5,11] We will also investigate a non-linear elastic FE model for modeling 3D gel rupture and needle–tissue interaction dynamics. It is also planned to adapt the current setup to investigate the collision between the needle and the gel sample, since using the current setup is not possible to visualize the needle tip when it is not fully inserted in the gel sample. Furthermore, we will simulate needle insertion into a prostate phantom that incorporates the anatomy of the male pelvic region, i.e., prostate and surrounding structures that support it. As part of future work, we will also vary system parameters such as bevel angle, insertion speed and needle diameter. During the experiments, needle tip will be tracked using an ultrasound-based tracking algorithm. Subsequently, simulation results will be compared with experimental data. The results of future study can be used to show that such an FE model can predict needle deflection during prostate biopsy and brachytherapy procedures.

References

1. Hung WK, Ying M, Chan CM, Lam HS, Mak KL, Minimally invasive technology in the management of breast disease, *Breast Cancer*, **16**(1):23–29, 2009.

2. Jahya A, van der Heijden F, Misra S, Observations of three-dimensional needle deflection during insertion into soft tissue, in *Proceedings of the 4th IEEE/RAS-EMBS International Conference on Biomedical Robotics and Biomechatronics (BioRob)*, Rome, Italy, pp. 1205–1210, 2012.

3. Misra S, Reed KB, Douglas AS, Ramesh KT, Okamura AM, Needle-tissue interaction forces for bevel-tip steerable needles, in *Proceedings of 2nd Biennal IEEE/RAS-EMBS International Conference on Biomedical Robotics and Biomechatronics (BioRob)*, Scottsdale, USA, pp. 227–231, 2008.

4. Chinzei K, Hata N, Jolesz FA, Kikinis R, MR compatible surgical assist robot: System integration and preliminary feasibility study, in *Proceedings of the International Conference on Medical Image Computing and Computer-Assisted Intervention (MICCAI)*, Pittsburgh, USA, pp. 921–930, 2000.

5. Abayazid M, Roesthuis RJ, and Reilink R, Misra S, Integrating deflection models and image feedback for real-time flexible needle steering, *IEEE Trans Robot* **29**(2):542–553, 2013.

6. DiMaio SP, Salcudean, SE, Needle insertion modeling and simulation, *IEEE Transactions on Robot Autom* **19**(5):864–875, 2003.

7. Kataoka H, Washio T, Chinzei K, Mizuhara K, Simone C, Okamura AM, Measurement of the tip and friction force acting on a needle during penetration, in *Proceedings of the International Conference on Medical Image Computing and Computer-Assisted Intervention (MICCAI)*, Tokyo, Japan, pp. 216–223, 2002.

8. Okamura AM, Simone C, O'Leary MD, Force modeling for needle insertion into soft tissue, *IEEE Trans Biomed Eng* **51**(10):1707–1716, 2004.

9. Podder TK, Clark DP, Fuller D, Sherman J, Ng WS, Liao L, Rubens DJ, Strang JG, Messing EM, Zhang YD, Yu Y, Effects of velocity modulation during surgical needle insertion, *Proc IEEE Int Conf Engineering in Medicine and Biology Society (EMBC)*, Shanghai, China, pp. 5766–5770, 2005.

10. Abolhassani N, Patel RV, Moallem M, Needle insertion into soft tissue: A survey, *Med Eng Phys* **29**(4):413–431, 2007.

11. Misra S, Reed KB, Schafer BW, Ramesh KT, Okamura AM, Mechanics of flexible needles robotically steered through soft tissue, *Int J Robot Res* **29**(13):1640–1660, 2010.

12. Van Veen YRJ, Jahya A, Misra S, Macroscopic and microscopic observations of needle insertion into gels, *J Eng Medi* **226**(6):441–449, 2012.

13. Jahya A, Herink M, Misra S, A framework for predicting 3D prostate deformation in real time, *Int J Med Robot Comput Assisted Surgery* **9**(4):e52–e60, December 2013.

14. Oldfield M, Dini D, Giordano G, y Baena FR, Detailed finite element modelling of deep needle insertions into asoft tissue phantom using cohesive approach, *Comput Meth Biomech Biomed Eng* **16**(5):530–543, 2013.

15. Kong XQ, Zhou P, Wu CW, Numerical simulation of microneedles' insertion into skin, *Comput Meth Biomech Biomed Eng* **14**(9):827–835, 2011.

16. Misra S, Macura KJ, Ramesh KT, Okamura AM, The importance of organ geometry and boundary constraints for planning of medical interventions, *Med Eng Phys* **31**(2):195–206, 2009.

17. Op den Buijs J, Hansen HHG, Lopata RPG, de Korte CL, Misra S, Predicting target displacements using ultrasound elastography and finite element modeling, *IEEE Trans Biomed Eng* **58**(11):3143–3155, 2011.

18. Assaad W, Misra S, Combining ultrasound-based elasticity estimation and FE models to predict 3D target displacement, *Med Eng Phys* **35**(4):544–549, 2013.

19. Jahya A, Schouten MG, Fütterer JJ, Misra S, On the importance of modelling organ geometry and boundary conditions for predicting three-dimensional prostate deformation, *Comput Meth Biomech Biomed Eng* **17**(5):497–506, 2014.
20. Amos WB, White JG, How the confocal laser scanning microscope entered biological research, *Biol Cell* **95**(6):335–342, 2003.
21. Salloum M, Ma RH, Weeks D, Zhu L, Controlling nanoparticle delivery in magnetic nanoparticle hyperthermia for cancer treatment: Experimental study in agarose gel, *Int J Hyperthermia* **24**(4):337–345, 2008.
22. Varoni E, Tschon M, Palazzo B, Nitti P, Martini L, Rimondini L, Agarose gel as biomaterial or scaffold for implantation surgery: Characterization, histological and histomorphometric study on soft tissue response, *Connect Tissue Res* **53**(6):548–554, 2012.
23. Yamada H, Strength of biological materials, The Williams & Wilkins Company, Baltimore, USA, 1970.
24. Normoand V, Lootens DL, Amici E, Plucknett KP, Aymard P, New insight into agarose gel mechanical properties, *Biomacromolecules* **1**(4):730–738, 2000.
25. Miller K, Chinzei K, Orssengo G, Bednarz, P, Mechanical properties of brain tissue invivo; experiment and computer simulation, *J Biomech* **33**(11):1369–1376, 2000.
26. Miller K, Method of testing very soft biological tissues in compression, *J Biomech* **38**(1):153–158, 2005.
27. Rizzieri R, Baker FS, Donald AM, A study of the large strain deformation and failure behaviour of mixed biopolymer gels via in situ ESEM, *Polymer* **44**(19):5927–5935, 2003.
28. Miller K and Chinzei K, Mechanical properties of brain tissue in tension, *J Biomech* **35**(4):483–490, 2002.
29. Johnson GR, Cook WH, Fracture characteristics of three metals subjected to various strains, strain rates, temperatures and pressures, *Eng Fracture Mech* **21**(1):31–48, 1985.
30. Hillerborg A, Modeer M, Petersson PE, Analysis of crack formation and crack growth in concrete by means of fracture mechanics and finite elements, *Cement Concrete Res* **6**(6):773–782, 1976.
31. Dassault Systémes, ABAQUS user's manual: version 6.11, Simulia Corporation, Providence, USA, 2011.